Calibrating the Absorption Imaging of Cold Atoms under High Magnetic Fields

Yuqi Liu,[1,‡] Zhongchi Zhang,[1,‡] Shiwan Miao,[1] Zihan Zhao,[1] Huaichuan Wang,[1] Wenlan Chen,[1,2,3,*] and Jiazhong Hu[1,2,3,†]

[1] *Department of Physics and State Key Laboratory of Low Dimensional Quantum Physics, Tsinghua University, 100084 Beijing, China*

[2] *Frontier Science Center for Quantum Information, 100084 Beijing, China*

[3] *Collaborative Innovation Center of Quantum Matter, 100084 Beijing, China*

(Received 27 April 2023; revised 23 June 2023; accepted 23 June 2023; published 18 July 2023)

We develop a theoretical model for calibrating the absorption imaging of cold atoms under high magnetic fields. Particularly it also works when the hyperfine structure is decoupled and cannot provide good quantum numbers anymore. Compared with zero or low magnetic fields, for high magnetic fields the efficiency of the absorption imaging is lower, while an additional correction factor is required to obtain the absolute atom number under the Beer-Lambert law. Our model is based on the rate equations and can account for many experimental imperfections, such as Zeeman level crossing, off-resonant couplings, and low repumping efficiency. On the basis of this method, we can precisely calculate the correction factor for atom-number measurement without any empirical or fitting parameters. Meanwhile, we use a cold-atom apparatus based on ^{85}Rb to experimentally verify our model. In addition, we find our work can also serve as a benchmark to measure the polarization impurity of a circularly polarized laser beam with high sensitivity. We believe this work will be beneficial for most cold-atom experiments using absorption imaging.

DOI: 10.1103/PhysRevApplied.20.014037

I. INTRODUCTION

The cold-atom platform has become a thriving area of research in recent decades, offering a powerful tool for studying many-body physics [1–4] because of its unique ability to directly measure the density of atoms in both real space and momentum space [5,6]. A plethora of novel phenomena have been observed, including the momentum bimodal distribution in Bose-Einstein condensates [7–9], phonon dispersion [10–12], and the superfluid-to-Mott transition in optical-lattice systems [13–16]. Absorption imaging is the most commonly used technique to observe these phenomena, where the density distribution of atoms is obtained by detecting the absorption of near-resonant light by the atoms. When atomic transitions are not saturated, the Beer-Lambert law predicts that the transmission of light decreases exponentially with increasing atomic density. By comparing the transmission intensity with and without atoms, we can obtain the density distribution of atoms.

Magnetic fields also play a crucial role in cold-atom experiments. By adjusting the magnetic field, we can tune the scattering length via Feshbach resonance [17], where the scattering-state energy coincides with that of a bound molecular state in the closed channel. This ability has generated many novel phases and phenomena and has paved the way for new fields, including Bose-Einstein condensate (BEC) to Bardeen-Cooper-Schrieffer (BCS) crossover [18–21], Efimov physics [22–25], Feshbach dimers [26–28], degenerate molecules [29–32], and quench dynamics [33–38]. In addition, magnetic fields offer powerful tools beyond tuning the interaction strength, including the use of spin-orbit coupling [39–43], Raman-sideband cooling [44–46], and synthetic gauge fields [47–49].

However, absorption imaging is highly sensitive to the energy structure of the atoms [50], which can be strongly affected by magnetic fields. As a result of level crossing and lifting of hyperfine-level degeneracy, the result of absorption imaging with nonzero magnetic field can be significantly different from that with zero magnetic field due to the low pumping efficiency and changed dipole moments. Nevertheless, with the advancement of quantum simulation, a more-precise measurement of the atom number is required in a growing number of cases, such as the measurement of equations of state [51–55] and the quantum gas microscope [14,15]. Currently, an empirical formula is commonly used to calibrate absorption imaging by fitting it with experimental data [51,52], which may be complicated and limited by the accuracy of experiments.

*cwlaser@ultracold.cn

†hujiazhong01@ultracold.cn

‡Liu and Z. Zhang contributed equally to this work.

In this paper, we develop a numerical model to calculate the impact of nonzero magnetic fields on absorption imaging, and we experimentally verify this model by use of a cold-atom apparatus based on ^{85}Rb atoms. By taking into account the interplay among various factors, including Zeeman level crossing and shifting, the change of dipole moments, light polarization, and repumping efficiency, we can accurately determine the correction factor for the atom-number measurement and identify the optimal parameters for imaging purposes. Moreover, this model can also serve as a benchmark for assessing the polarization purity of light since absorption imaging with some specific apparatus is very sensitive to the polarization.

This paper is organized as follows: Sec. II provides a description of our theoretical model and includes a simplified illustration of how nonzero magnetic fields impact the imaging procedure. Section III presents our experimental demonstration, which provides consistent results with our numerical calculations. In addition, we give explanations for each peak and valley in the spectrum. In Sec. IV, we show that absorption imaging with nonzero magnetic fields can be used as a benchmark for evaluating the quality of circularly polarized light, where the sensitivity of the polarization impurity can reach the 0.02% level. It provides a practical application for inspecting the laser-beam polarization in a cold-atom apparatus without additional optics or instruments with high precision.

II. THEORETICAL MODEL FOR HIGH-FIELD IMAGING

In this section, we focus on the theoretical part of high-field imaging and divide the presentation into three parts. The first part is a brief summary of absorption imaging, which is the foundation of this work. The second part is a discussion of the challenges of high-field imaging. It explains why researchers obtain different optical depths or atom numbers under high magnetic fields. The third part explains how we use rate equations to describe the imaging process. On the basis of these equations, we calculate the imaging efficiency β.

A. A brief summary of absorption imaging

First, we provide a brief summary of absorption imaging. When a beam of light, $I_{\text{in}}(x,y)$, propagates parallel to the z axis and enters a sample of atoms, the modified Beer-Lambert law states that [56,57]

$$\frac{dI(x,y,z)}{dz} = -n(x,y,z)\sigma \frac{I(x,y,z)}{1+I(x,y,z)/I_{\text{sat}}}. \tag{1}$$

By measuring the laser intensity before and after the sample, we can calculate the optical depth $\mathcal{D}$, which is the product of the absorption cross section σ and the area density $n_{2D}(x,y) = \int_{-\infty}^{+\infty} n(x,y,z)dz$, as

$$\mathcal{D}(x,y) = n_{2\text{D}}(x,y)\sigma = -\ln\left[\frac{I_{\text{final}}(x,y)}{I_{\text{in}}(x,y)}\right] + \frac{I_{\text{in}} - I_{\text{final}}}{I_{\text{sat}}}. \tag{2}$$

The absorption cross section, σ, is defined as

$$\sigma = \frac{\hbar\omega\Gamma}{2I_{\text{sat}}} \frac{1}{1+4(\Delta/\Gamma)^2}, \tag{3}$$

where $\Delta = \omega - \omega_0$ is the detuning between the imaging light frequency ω and the atomic resonance ω_0, and Γ is the spontaneous emission rate. The saturation intensity, I_{sat}, can be calculated by

$$I_{\text{sat}} = \frac{c\epsilon_0\Gamma^2\hbar^2}{4|\hat{\mathbf{p}}\cdot\mathbf{d}|^2}, \tag{4}$$

where ϵ_0 is the vacuum dielectric constant, c is the speed of light, $\hat{\mathbf{p}}$ is the unit polarization vector of the light field, and $\mathbf{d}$ is the dipole moment. In the following paragraphs, we use the atomic total angular momentum, F, and its projection on the quantization axis (z axis), m_F, to label a ground state $|s\rangle = |F, m_F\rangle$ or an excited state $|s'\rangle = |F', m'_F\rangle$, where the prime indicates an excited state. The dipole moment of alkali atoms between state $|s\rangle$ and state $|s'\rangle$ can be calculated by the formula

$$d_{|s\rangle,|s'\rangle,p} = \alpha_{|s\rangle,|s'\rangle,p}\sqrt{\frac{2J+1}{2J'+1}}\langle J||e\mathbf{r}||J'\rangle, \tag{5}$$

where J and J' label the total electronic spin, $\langle J||e\mathbf{r}||J'\rangle$ is the transition-dipole-matrix element, which can be found in data sheets [58], and $\alpha_{|s\rangle,|s'\rangle,p}$ is a coefficient. The subscript p here denotes the projection into the unit polarization vector $\hat{\mathbf{p}}$ of the light field.

For better illustration, we chose ^{85}Rb atoms to demonstrate the energy levels in detail. This choice does not affect the generality of our results. In Fig. 1, we present a conventional experimental setup with the energy-level structure. We list the square of the dipole-moment coefficient, $|\alpha_{|s\rangle,|s'\rangle}|^2 = |\sum_p \alpha_{|s\rangle,|s'\rangle,p}|^2$, for some transitions of ^{85}Rb under zero magnetic field in Table I. Typically, a closed transition is used to maximize the photon scattering of the imaging beam. In this transition, the excited state can decay only to one ground state. For ^{85}Rb, the closed transition is the transition between $5S_{1/2}|3,-3\rangle$ and $5P_{3/2}|4',-4'\rangle$ for an imaging beam with a σ^- polarization.

When the magnetic field is small such the Zeeman splitting is less than the spontaneous-emission rate, we can ignore the change of light detunings between the ground and excited states due to Zeeman shift. All atoms in the $F = 3$ manifold can be excited by the imaging

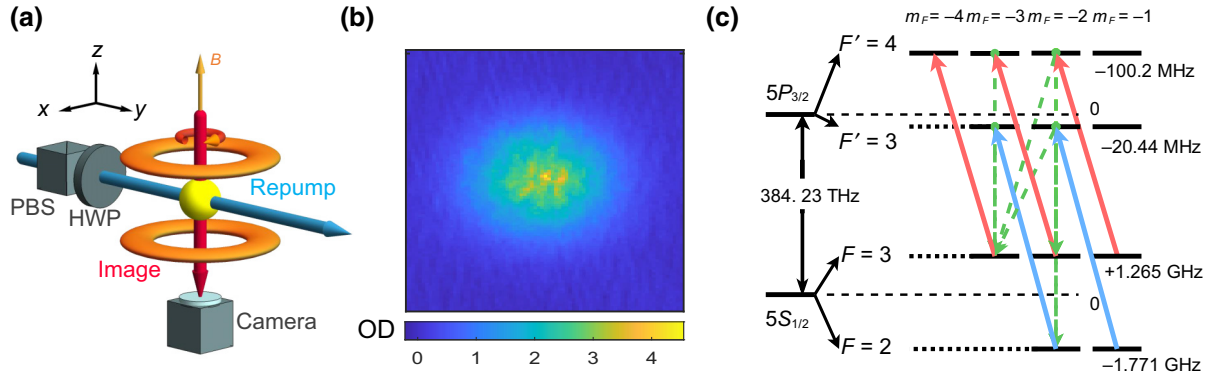

FIG. 1. (a) A conventional experimental setup for absorption imaging. A pair of Helmholtz coils generate a magnetic field along the z axis. The imaging beam is sent into a camera along the z axis with circular polarization σ^-. Besides the imaging beam, a repumping beam is required to clean the other hyperfine levels in ground-state manifolds. Here we send the repumping beam along the y axis to avoid it entering the camera. (b) An absorption image obtained in our experiment and the optical depth calculated by the Beer-Lambert law. (c) Part of the energy levels of ^{85}Rb under zero magnetic field. Red arrows correspond to the imaging light, blue arrows correspond to the repumping light, and dashed green arrows correspond to the spontaneous emission. After a few spontaneous decays, the atomic population accumulates in the state $5S_{1/2}|3,-3\rangle$ with a closed transition to $5P_{3/2}|4',-4'\rangle$ for the imaging light. HWP, half-wave plate; OD, optical depth; PBS, polarizing beam splitter.

light with a σ^- polarization [red arrows in Fig. 1(c)], which also connects the closed transition $5S_{1/2}|3,-3\rangle \rightarrow 5P_{3/2}|4',-4'\rangle$. However, atoms may also initially occupy the ground states with $F = 2$, so a repumping beam (blue arrows) is required to resonantly pump atoms from the $F = 2$ manifold to the $F = 3$ manifold via the excited states with $F' = 3$. After several spontaneous emissions, all atoms will be initialized in the closed transition with $5S_{1/2}|3,-3\rangle$, regardless of any initial populations in ground states.

B. Difficulties of imaging under high magnetic fields

Under high magnetic fields, the Zeeman energy shift becomes larger than the spontaneous-emission rate, and the total angular momentum F describing the hyperfine structure is no longer a good quantum number. In particular, the $5P_{3/2}$ manifold of excited states is strongly mixed by magnetic fields since the hyperfine splitting for excited states is much smaller than that of ground states. Therefore, we need to rediagonalize the eigenstates under both magnetic fields and hyperfine interactions.

In the absence of a magnetic field, we use the hyperfine structure $|F, m_F\rangle$ to identify the eigenstates. However, at nonzero magnetic fields, the total angular momentum F is not a good quantum number anymore. To label the states that are adiabatically connected to the zero-field state $|F, m_F\rangle$, we use the notation $|\tilde{F}, \tilde{m}_F\rangle$. At very high magnetic fields, where the Zeeman splitting greatly exceeds the hyperfine splitting, the states $|\tilde{F}, \tilde{m}_F\rangle$ are actually labeled by another set of good quantum numbers $|m_J, m_I\rangle$, where m_J and m_I are the angular momenta of electrons and nuclei along the magnetic field. We plot the energy levels versus the magnetic field for the $5P_{3/2}$ manifold in Fig. 2(a). The dipole moments between different states are also affected by the magnetic field, and we provide the square of the dipole-moment coefficients ($|\alpha|^2$) of ^{85}Rb under a magnetic field of 161 G in Table II for comparison.

As the magnetic field increases, the dipole moments between different states are strongly distorted, and this has a significant impact on the frequencies of the repumping lasers that we choose. For example, the transition $5P_{3/2}|\tilde{3}',-\tilde{3}'\rangle \rightarrow 5S_{1/2}|\tilde{3},-\tilde{3}\rangle$ is strongly suppressed due to different nuclear spins at high field. However, some dipole transitions that are forbidden under zero magnetic field become no longer forbidden, such as the transition $5S_{1/2}|\tilde{2},-\tilde{2}\rangle \rightarrow 5P_{3/2}|\tilde{4}',-\tilde{3}'\rangle$. Meanwhile, the closed transition $5P_{3/2}|\tilde{4}',-\tilde{4}'\rangle \rightarrow 5S_{1/2}|\tilde{3},-\tilde{3}\rangle$ is not affected by the magnetic field since the hyperfine states involved in this transition do not change with respect to the magnetic

TABLE I. The square of the dipole-moment coefficients $|\boldsymbol{\alpha}|^2$ between the manifolds of $5^2P_{3/2}$ and $5^2S_{1/2}$ in ^{85}Rb under zero magnetic field.

	$5S_{1/2}$				
$5P_{3/2}$	$\|3,-3\rangle$	$\|3,-2\rangle$	$\|2,-2\rangle$	$\|3,-1\rangle$	$\|2,-1\rangle$
$\|4',-4'\rangle$	1	0	0	0	0
$\|4',-3'\rangle$	1/4	3/4	0	0	0
$\|3',-3'\rangle$	5/12	5/36	4/9	0	0
$\|4',-2'\rangle$	1/28	3/7	0	15/28	0
$\|3',-2'\rangle$	5/36	5/27	4/27	25/108	7/18
$\|2',-2'\rangle$	10/63	10/189	14/27	2/189	7/27
$\|4',-1'\rangle$	0	3/28	0	15/28	0
$\|3',-1'\rangle$	0	25/108	4/135	5/108	32/135
$\|2',-1'\rangle$	0	20/189	7/27	16/189	7/54
$\|1',-1'\rangle$	0	0	3/5	0	3/10

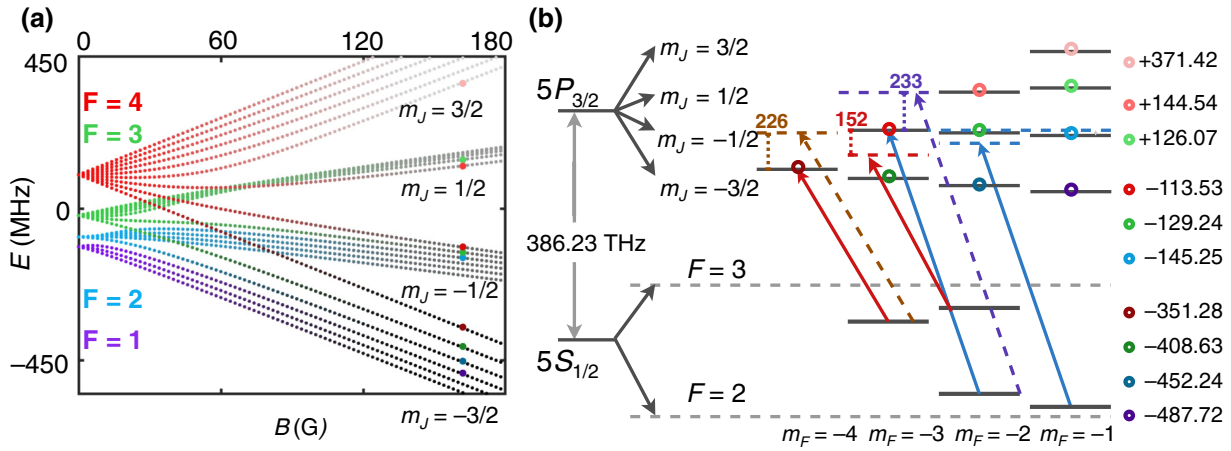

FIG. 2. (a) Energy levels of the ^{85}Rb $5P_{3/2}$ state plotted for different magnetic fields. The angular momentum along the z axis of the displayed levels ranges from -4 to -1. The filled circles mark the levels at a magnetic field of 161 G, with the energy given on the right in the unit of megahertz. (b) Atomic structure at 161 G. Solid red arrows and solid blue arrows represent the imaging light and the repumping light, respectively. The dashed brown arrows and dashed purple arrows correspond to the imaging light and the repumping light, respectively, in the absence of a magnetic field. The imaging light and the repumping light require red detuning by 226 and 233 MHz to change to the magnetic field. Specifically, the imaging light has a red detuning of 152 MHz for the transition between $5^2S_{1/2}|3,-2\rangle$ and $5^2P_{3/2}|4',-3'\rangle$.

field. Therefore, under high magnetic fields, we should set the repumping light to be resonant with the transition $5S_{1/2}|\tilde{2},-\tilde{2}\rangle \rightarrow 5P_{3/2}|\tilde{4}',-\tilde{3}'\rangle$ instead of $5P_{3/2}|\tilde{3}',-\tilde{3}'\rangle$ to initialize most of the atoms in the state $5S_{1/2}|\tilde{3},-\tilde{3}\rangle$ (Fig. 2). This is a significant difference in repumping between zero and high magnetic fields.

However, the absorption-imaging efficiency is still lower than that under zero magnetic field. This is because some of the atoms pumped from $5S_{1/2}|\tilde{2},-\tilde{2}\rangle$ to $5P_{3/2}|\tilde{4}',-\tilde{3}'\rangle$ will decay to $5S_{1/2}|\tilde{3},-\tilde{2}\rangle$ instead of $5S_{1/2}|\tilde{3},-\tilde{3}\rangle$. In the absence of a magnetic field, the degeneracy of the $F=3$ manifold ensures that atoms in $5S_{1/2}|\tilde{3},-\tilde{2}\rangle$ will be pumped by the imaging beam and ultimately decay to the state $5S_{1/2}|\tilde{3},-\tilde{3}\rangle$. However, under a high magnetic field, atoms scattering to $5S_{1/2}|\tilde{3},-\tilde{2}\rangle$ can

TABLE II. The square of the dipole-moment coefficients $|\boldsymbol{\alpha}|^2$ between manifolds $5P_{3/2}$ and $5S_{1/2}$ of ^{85}Rb under a magnetic field of 161 G. We label $5P_{3/2}$ states by both $|m_J',m_I'\rangle$ and $|\tilde{F}',\tilde{m}_F'\rangle$.

$5P_{3/2}$ $\lvert\tilde{F}',\tilde{m}_F'\rangle$ ($\lvert m_J',m_I'\rangle$)	$5S_{1/2}$ $\lvert\tilde{F},\tilde{m}_F\rangle$				
	$\lvert\tilde{3},-\tilde{3}\rangle$	$\lvert\tilde{3},-\tilde{2}\rangle$	$\lvert\tilde{2},-\tilde{2}\rangle$	$\lvert\tilde{3},-\tilde{1}\rangle$	$\lvert\tilde{2},-\tilde{1}\rangle$
$\lvert\tilde{4}',-\tilde{4}'\rangle$ $\left(\left\lvert-\frac{3}{2}',-\frac{5}{2}'\right\rangle\right)$	1	0	0	0	0
$\lvert\tilde{4}',-\tilde{3}'\rangle$ $\left(\left\lvert-\frac{1}{2}',-\frac{5}{2}'\right\rangle\right)$	0.6394	0.1945	0.1660	0	0
$\lvert\tilde{3}',-\tilde{3}'\rangle$ $\left(\left\lvert-\frac{3}{2}',-\frac{3}{2}'\right\rangle\right)$	0.0272	0.6624	0.3104	0	0
$\lvert\tilde{4}',-\tilde{2}'\rangle$ $\left(\left\lvert+\frac{1}{2}',-\frac{5}{2}'\right\rangle\right)$	0.3163	0.2804	0.3852	0.0125	0.0056
$\lvert\tilde{3}',-\tilde{2}'\rangle$ $\left(\left\lvert-\frac{1}{2}',-\frac{3}{2}'\right\rangle\right)$	0.0170	0.3648	0.2743	0.2566	0.0873
$\lvert\tilde{2}',-\tilde{2}'\rangle$ $\left(\left\lvert-\frac{3}{2}',-\frac{1}{2}'\right\rangle\right)$	2.3×10^{-5}	0.0215	0.0071	0.4617	0.5097
$\lvert\tilde{4}',-\tilde{1}'\rangle$ $\left(\left\lvert+\frac{3}{2}',-\frac{5}{2}'\right\rangle\right)$	0	0.2952	0.6840	0.0126	0.0077
$\lvert\tilde{3}',-\tilde{1}'\rangle$ $\left(\left\lvert+\frac{1}{2}',-\frac{3}{2}'\right\rangle\right)$	0	0.1657	0.1678	0.4195	0.2259
$\lvert\tilde{2}',-\tilde{1}'\rangle$ $\left(\left\lvert-\frac{1}{2}',-\frac{1}{2}'\right\rangle\right)$	0	0.0155	0.0051	0.2218	0.4232
$\lvert\tilde{1}',-\tilde{1}'\rangle$ $\left(\left\lvert-\frac{3}{2}',+\frac{1}{2}'\right\rangle\right)$	0	1.3×10^{-5}	2.2×10^{-7}	0.0128	0.0099

hardly be pumped to the $5P_{3/2}|\tilde{4}', -\tilde{3}'\rangle$ state due to the large detuning [152 MHz at 161 G in Fig. 2(b)]. As a result, only atoms in the $5S_{1/2}|\tilde{3}, -\tilde{3}\rangle$ state can be imaged by the imaging light, leading to a reduction in the absorption-imaging efficiency. To account for this, an additional coefficient (or efficiency) β ($\beta < 1$) is required to correct the optical depth and accurately reflect the real atom number in the Beer-Lambert law, which can be expressed as

$$n(x,y)\sigma\beta = \mathcal{D}(x,y). \tag{6}$$

Therefore, accurately predicting and calculating how the efficiency β changes with respect to the magnetic field strength is crucial for high-field imaging.

C. Rate equations describing high-field imaging

In this section, we develop a model for calculating the efficiency β of absorption imaging. According to the definition of β, we can calculate it as follows:

$$\beta = dN_{\rm img}/dN_{\rm img,0\,G}, \tag{7}$$

where $dN_{\rm img}$ is the mean number of photons in the imaging beam scattered by one atom under a particular magnetic field in a time duration $d\tau$, and $dN_{\rm img,0\,G}$ is the mean photon number scattered by the same atom under the same conditions, except that there is no magnetic field. Our model simulates the process in which an ensemble of atoms is illuminated by repumping light with intensity $I_{\rm rep}$ and imaging light with intensity $I_{\rm img}$. We use a vector

$$\mathbf{v}_{\rm oc} = \{f_{|F',m'_F\rangle}, \ldots, f_{|F,m_F\rangle}, \ldots\}^T \tag{8}$$

to list the population fraction of all energy levels related to the imaging process. Here, $f_{|F',m'_F\rangle}$ is the fraction of atoms occupying the state $|F', m'_F\rangle$ in the ensemble, and the superscript T means a transposed matrix. The sum of all occupation fractions $f_{|s\rangle}$ and $f_{|s'\rangle}$ is 1. The variation of $\mathbf{v}_{\rm oc}$ obeys a rate equation:

$$\frac{d\mathbf{v}_{\rm oc}}{dt} = \mathbf{M}_T\mathbf{v}_{\rm oc}. \tag{9}$$

To obtain the exact form of this rate equation, we write down each equation for both excited and ground states with forms of

$$\frac{df_{|s\rangle}}{dt} = -\sum_{l,j,p}\left(\frac{\Gamma_{|s'_j\rangle}}{2}\right)\frac{|\alpha_{p,|s\rangle,|s'_j\rangle}|^2 I_{l,p}/I_{\rm sat}}{1+4(\Delta_{l,|s\rangle,|s'_j\rangle}/\Gamma_{|s'_j\rangle})^2}(f_{|s\rangle} - f_{|s'_j\rangle}) + \sum_j \Gamma_{|s'_j\rangle}|\boldsymbol{\alpha}_{|s\rangle,|s'_j\rangle}|^2 f_{|s'_j\rangle} \tag{10}$$

and

$$\frac{df_{|s'\rangle}}{dt} = +\sum_{l,i,p}\left(\frac{\Gamma_{|s'\rangle}}{2}\right)\frac{|\alpha_{p,|s\rangle,|s'_j\rangle}|^2 I_{l,p}/I_{\rm sat}}{1+4(\Delta_{l,|s_i\rangle,|s'\rangle}/\Gamma_{|s'\rangle})^2}(f_{|s_i\rangle} - f_{|s'\rangle}) - \Gamma_{|s'\rangle}f_{|s'\rangle}. \tag{11}$$

Here l is used to label different beams in the system, $I_{\rm sat}$ represents the saturation intensity calculated with Eq. (4) with a specific substitution $|\hat{\mathbf{p}}\cdot\mathbf{d}_{|s\rangle,|s'\rangle}| = \sqrt{(2J+1)/(2J'+1)}\langle J||e\mathbf{r}||J'\rangle$, $I_{l,p}$ is the p-polarized intensity of the lth beam, and $\Delta_{l,|s\rangle,|s'\rangle}$ is the detuning between the lth beam and the transition $|s\rangle \to |s'\rangle$. The average photon number $dN_{\rm img}$ scattered by one atom at time t in time duration $d\tau$ is given by

$$\frac{dN_{\rm img}(t)}{d\tau} = \sum_{|s\rangle,|s'\rangle,p}\left(\frac{\Gamma_{|s'\rangle}}{2}\right)\frac{\alpha^2_{|s\rangle,|s'\rangle,p} I_{{\rm img},p}/I_{\rm sat,ref}}{1+4(\Delta_{{\rm img},|s\rangle,|s'\rangle}/\Gamma_{|s'\rangle})^2} \times \left(f_{|s\rangle}(t) - f_{|s'\rangle}(t)\right). \tag{12}$$

The vector $\mathbf{v}_{\rm oc}$ and the transition matrix $\mathbf{M}_T$ are written in the partitioned form,

$$\mathbf{v}_{\rm oc} = \{\mathbf{v}_{|s'\rangle}, \mathbf{v}_{|s\rangle}\}^T, \tag{13}$$

$$\mathbf{M}_t = \begin{bmatrix} \mathbf{M}_{s's'} & \mathbf{M}_{\rm sti} \\ \mathbf{M}^T_{\rm sti} + \mathbf{M}_{\rm spon} & \mathbf{M}_{ss} \end{bmatrix}, \tag{14}$$

where $\mathbf{v}_{|s'\rangle}$ and $\mathbf{v}_{|s\rangle}$ describe the population fractions of the excited-state and ground-state manifolds, respectively. According to Eqs. (10) and (11), the submatrices of $\mathbf{M}_T$ can be expressed as follows:

$$\begin{aligned}
[\mathbf{M}_{\rm sti}]_{|s'_j\rangle,|s_i\rangle} &= \sum_{l,p}\left(\frac{\Gamma_{|s'_j\rangle}}{2}\right)\frac{|\alpha_{p,|s\rangle,|s'_j\rangle}|^2 I_{l,p}/I_{\rm sat}}{1+4(\Delta_{l,|s_j\rangle,|s'_i\rangle}/\Gamma_{|s'_i\rangle})^2}, \\
\left[\mathbf{M}_{\rm spon}\right]_{|s_i\rangle,|s'_j\rangle} &= \Gamma_{|s'_j\rangle}|\boldsymbol{\alpha}_{|s\rangle,|s'_j\rangle}|^2, \\
[\mathbf{M}_{ss}]_{|s_i\rangle,|s_k\rangle} &= -\delta_{ik}\sum_j [\mathbf{M}_{\rm sti}]_{|s'_j\rangle,|s_i\rangle}, \\
[\mathbf{M}_{s's'}]_{|s'_j\rangle,|s'_k\rangle} &= -\delta_{jk}\sum_i [\mathbf{M}_{\rm sti}]_{|s'_j\rangle,|s_i\rangle} - \delta_{jk}\Gamma_{|s'_j\rangle},
\end{aligned} \tag{15}$$

where δ_{ik} is a Kronecker-δ symbol. On the basis of the rate equations, we calculate $dN_{\rm img}/d\tau$ for atoms with and without a magnetic field, which leads to the coefficient β in Eq. (7). We have developed a package of codes that can calculate dipole-moment coefficients $\alpha_{|s\rangle,|s'\rangle}$, the transition matrix $\mathbf{M}_T$, and rate equations. These codes can be obtained through a public code deposit service [59].

After deriving the rate equations, we illustrate the evolution of atomic populations over time and the resulting efficiency β. Figure 3(a) depicts the time-dependent populations of states $5S_{1/2}|\tilde{3},-\tilde{3}\rangle$, $5S_{1/2}|\tilde{3},-\tilde{2}\rangle$, $5S_{1/2}|\tilde{2},-\tilde{2}\rangle$, and $5P_{3/2}|\tilde{4}',-\tilde{4}'\rangle$ at a magnetic field of 161 G, with $I_{\rm img}$ and $I_{\rm rep}$ set to $1.1I_{\rm sat}$ and $0.6I_{\rm sat}$. The imaging beam is polarized as σ_-, while the repumping beam is polarized as half σ_+ and half σ_-. Initially, all atoms are prepared in the state $5S_{1/2}|\tilde{2},-\tilde{2}\rangle$. The population of $5S_{1/2}|\tilde{2},-\tilde{2}\rangle$ drops to zero within 10 μs, and most of the atoms enter the closed cycle for imaging with an efficiency of approximately 75%. However, some of the atoms enter other states, as shown in Fig. 3(a). To further analyze the early transient behaviors, we introduce a settling time τ_s, defined as the time for the decay of $f_{|\tilde{2},-\tilde{2}\rangle}$ from 1 to $1/e^2$. Once the imaging time exceeds τ_s, the transient behaviors can be disregarded. In Fig. 3(b), we plot τ_s against $I_{\rm rep}$, demonstrating that the settling time is less than 10 μs when $I_{\rm rep}$ exceeds $0.2I_{\rm sat}$ under a magnetic field of 161 G. We also compare the results at 161 and 0 G, revealing no order difference in the settling time with or without a magnetic field.

Figure 3(c) displays the efficiency β versus $I_{\rm rep}$ with an imaging time of 40 μs, indicating how the transient behaviors of population repumping affect β. We observe that β changes by 11% in the intensity range from $0.1I_{\rm sat}$ to $I_{\rm sat}$ due to the change of repumping efficiency. When the intensity of the repumping light is larger than $I_{\rm sat}$, the change of β is less than 1%. Figure 3(d) displays the variation of β with respect to the imaging intensity $I_{\rm img}$. It can be observed that in the intensity range from $0.1I_{\rm sat}$ to $1.5I_{\rm sat}$, the change in β is only 1.4%. Therefore, it is a good approximation that the efficiency β is independent of the imaging intensity. In most experiments, the imaging light is attenuated by atoms due to a large optical depth, resulting in different light intensities being experienced by each atom. However, the high repumping efficiency under a high magnetic field enables the imaging process with the repumping transition $5S_{1/2}|\tilde{2},-\tilde{2}\rangle \rightarrow 5P_{1/2}|\tilde{4}',-\tilde{3}'\rangle$ to have saturation intensity similar to that in the case without a magnetic field. As shown in Fig. 3(d), the efficiency β can be treated as approximately constant, at least to the leading order. Therefore, a universal β can be used to describe the imaging process, provided that a precise measurement of the light intensity is not required.

Figure 4 shows the variation of β with respect to the magnetic field ranging from 0 to 180 G. The solid curves represent the theoretical calculations, while the scattered points correspond to the experimental data. These curves are further elaborated in the next section, in conjunction with the experimental procedures.

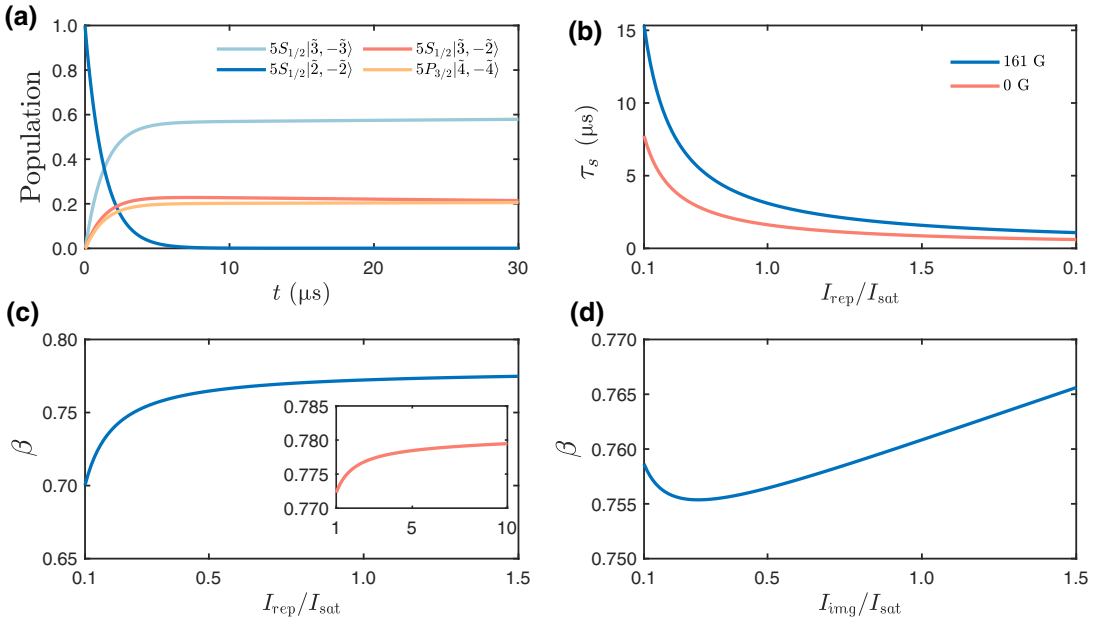

FIG. 3. (a) Temporal evolution of the populations of the four main states, namely, $5S_{1/2}|\tilde{3},-\tilde{3}\rangle$, $5S_{1/2}|\tilde{3},-\tilde{2}\rangle$, $5S_{1/2}|\tilde{2},-\tilde{2}\rangle$, and $5P_{3/2}|\tilde{4}',-\tilde{4}'\rangle$, under the conditions of a magnetic field of 161 G, $I_{\rm img} = 1.1I_{\rm sat}$, and $I_{\rm rep} = 0.6I_{\rm sat}$. (b) Settling time τ_s versus repumping-light intensity $I_{\rm rep}$ for magnetic fields of 0 and 161 G. (c) Imaging efficiency β versus repumping-light intensity $I_{\rm rep}$ under a magnetic field of 161 G and an imaging duration of 40 μs . The main plot shows the range from $0.1I_{\rm sat}$ to $1.5I_{\rm sat}$, and the inset shows the range from $I_{\rm sat}$ to $10I_{\rm sat}$. When the repumping-light intensity reaches the saturation intensity, the efficiency β experiences a negligible change of less than 1%. (d) Efficiency β versus imaging-light intensity $I_{\rm img}$ under a magnetic field of 161 G and an imaging duration of 40 μs. The change of β is less than 1.4%.

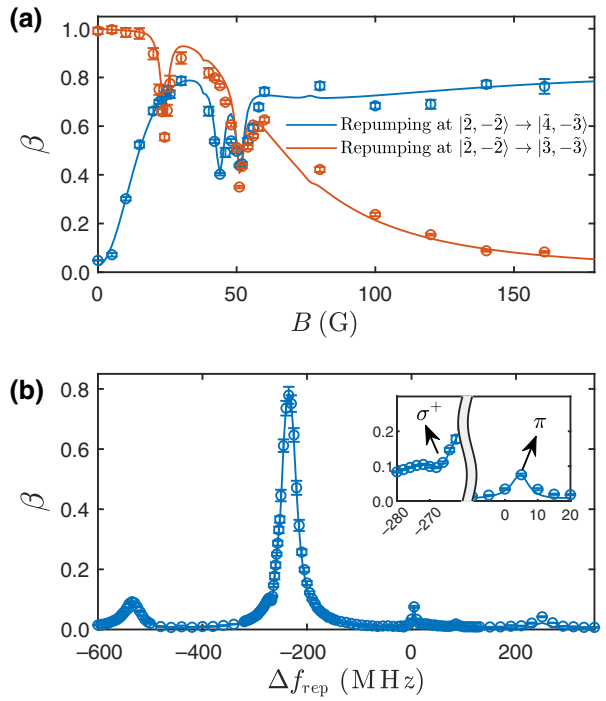

FIG. 4. (a) Imaging efficiency β versus magnetic field with two different repumping frequencies. The solid curves are theoretical calculations and the scattered points are the experimental data, while the error bars correspond to 1 standard deviation. Each data point corresponds to the average of ten experimental measurements. The red curve and red points correspond to the repumping transition $5S_{1/2}|\tilde{2},-\tilde{2}\rangle \rightarrow 5P_{3/2}|\tilde{3}',-\tilde{3}'\rangle$. The blue curve and blue points correspond to the repumping transition $5S_{1/2}|2,-2\rangle \rightarrow 5P_{3/2}|\tilde{4}',-\tilde{3}'\rangle$. (b) β versus repumping frequency under a magnetic field of 161 G. Here the frequency zero point corresponds to the frequency of the transition $5S_{1/2}|\tilde{2},-\tilde{2}\rangle \rightarrow 5P_{3/2}|\tilde{3}',-\tilde{3}'\rangle$ under a magnetic field of 0 G. There are two large peaks, at -535 and -235 MHz, corresponding to the transition $5S_{1/2}|\tilde{2},-\tilde{2}\rangle \rightarrow 5P_{3/2}|\tilde{3}',-\tilde{3}'\rangle$ and the transition $5S_{1/2}|\tilde{2},-\tilde{2}\rangle \rightarrow 5P_{3/2}|\tilde{4}',-\tilde{3}'\rangle$. The inset shows in more detail features around -270 and 0 MHz, and shows that there is a peak at 5 MHz and a valley at -268 MHz, which are attributed to the π component and the σ^+ component of the repumping light.

III. EXPERIMENTAL VERIFICATION

Our experimental setup, depicted in Fig. 1(a), uses a crossed dipole trap with vibrational frequencies $\omega_x/2\pi =$ 180 Hz, $\omega_y/2\pi = 180$ Hz, and $\omega_z/2\pi = 255$ Hz to confine 1.3×10^6 ^{85}Rb atoms. The atoms are initially prepared in the state $5S_{1/2}|2,-2\rangle$, which exhibits a broad Feshbach resonance at approximately 155 G. Before the subsequent experiment, the atoms are allowed to reach thermal equilibrium at a temperature of 10 μK. The magnetic field is then adiabatically raised to the desired value and held for 400 ms, after which the dipole trap is turned off and the atoms are allowed to expand for the time-of-flight measurement. We then conduct absorption imaging at the target magnetic field using imaging light with $I_{\text{img}} = 1.1I_{\text{sat}}$ and repumping light with $I_{\text{rep}} = 0.6I_{\text{sat}}$. The imaging light is predominantly polarized in the σ^- direction, while the repumping light with a linear polarization perpendicular to the magnetic field is split evenly between σ^+ and σ^-. For comparison, we also need to perform the absorption imaging at zero magnetic field to determine the actual atom number. Because of different losses under different magnetic fields, we also ramp up the magnetic field to the desired value, then hold atoms for the same time, and then ramp down the magnetic field to zero for imaging. This ensures that the atoms experience the same loss process at both high magnetic fields and zero magnetic field. By comparing these two results, we can get the efficiency β.

In Fig. 4(a), we compare two cases with different repumping frequencies at desired magnetic fields. One is resonant with the transition $5S_{1/2}|\tilde{2},-\tilde{2}\rangle \rightarrow 5P_{3/2}|\tilde{3}',-\tilde{3}'\rangle$ (red curve and points) and the other is resonant with the transition $5S_{1/2}|\tilde{2},-\tilde{2}\rangle \rightarrow 5P_{3/2}|\tilde{4}',-\tilde{3}'\rangle$ (blue curve and points). Under zero magnetic field, the transition $5S_{1/2}|\tilde{2},-\tilde{2}\rangle \rightarrow 5P_{3/2}|\tilde{4}',-\tilde{3}'\rangle$ is dipole forbidden, so the efficiency β is zero. As the magnetic field increases, the transition $5S_{1/2}|\tilde{2},-\tilde{2}\rangle \rightarrow 5P_{3/2}|\tilde{4}',-\tilde{3}'\rangle$ becomes increasingly allowed, resulting in a higher β. Meanwhile, the σ^+ polarization of the repumping light, which would pump the atoms to levels further away from the closed transition, is supposed to decrease β. Therefore, β of the repumping frequency $5S_{1/2}|\tilde{2},-\tilde{2}\rangle \rightarrow 5P_{3/2}|\tilde{4}',-\tilde{3}'\rangle$ has a valley at 44 G due to the level crossing of $5P_{3/2}|\tilde{4}',-\tilde{3}'\rangle$ and $5P_{3/2}|\tilde{3}',-\tilde{1}'\rangle$, and β of the repumping frequency $5S_{1/2}|\tilde{2},-\tilde{2}\rangle \rightarrow 5P_{3/2}|\tilde{3}',-\tilde{3}'\rangle$ has a valley at 21 G due to the crossing of $5P_{3/2}|\tilde{3}',-\tilde{3}'\rangle$ and $5P_{3/2}|\tilde{2}',-\tilde{1}'\rangle$. Similarly, both transitions exhibit a valley in their efficiency at 51 G where the energies of $5P_{3/2}|\tilde{4}',-\tilde{4}'\rangle$ and $5P_{3/2}|\tilde{3}',-\tilde{2}'\rangle$ cross, due to the residual σ^+ polarization of the imaging light.

In Fig. 4(b), we show the efficiency β versus the repumping-light frequency at 161 G. The frequency zero point is defined as the transition $5S_{1/2}|\tilde{2},-\tilde{2}\rangle \rightarrow 5P_{3/2}|\tilde{3}',-\tilde{3}'\rangle$ under zero magnetic field. The peaks at -530 and -235 MHz correspond to the transitions $5S_{1/2}|\tilde{2},-\tilde{2}\rangle \rightarrow 5P_{3/2}|\tilde{3}',-\tilde{3}'\rangle$ and $5S_{1/2}|\tilde{2},-\tilde{2}\rangle \rightarrow 5P_{3/2}|\tilde{4}',-\tilde{3}'\rangle$, respectively, and are due to the σ^- component of the repumping light. We can clearly see that the transition $5S_{1/2}|\tilde{2},-\tilde{2}\rangle \rightarrow 5P_{3/2}|\tilde{4}',-\tilde{3}'\rangle$ corresponds to the most-efficient repumping frequency at high magnetic field and gives β of 0.78. The peak at 250 MHz and the valley at -268 MHz correspond to the transitions $5S_{1/2}|\tilde{2},-\tilde{2}\rangle \rightarrow 5P_{3/2}|\tilde{4}',-\tilde{1}'\rangle$ and $5S_{1/2}|\tilde{2},-\tilde{2}\rangle \rightarrow 5P_{3/2}|\tilde{2}',-\tilde{1}'\rangle$, respectively, and are due to the σ^+ component of the repumping light. The small peak at 5 MHz corresponds to the transition $5S_{1/2}|\tilde{2},-\tilde{2}\rangle \rightarrow 5P_{3/2}|\tilde{4}',-\tilde{2}'\rangle$

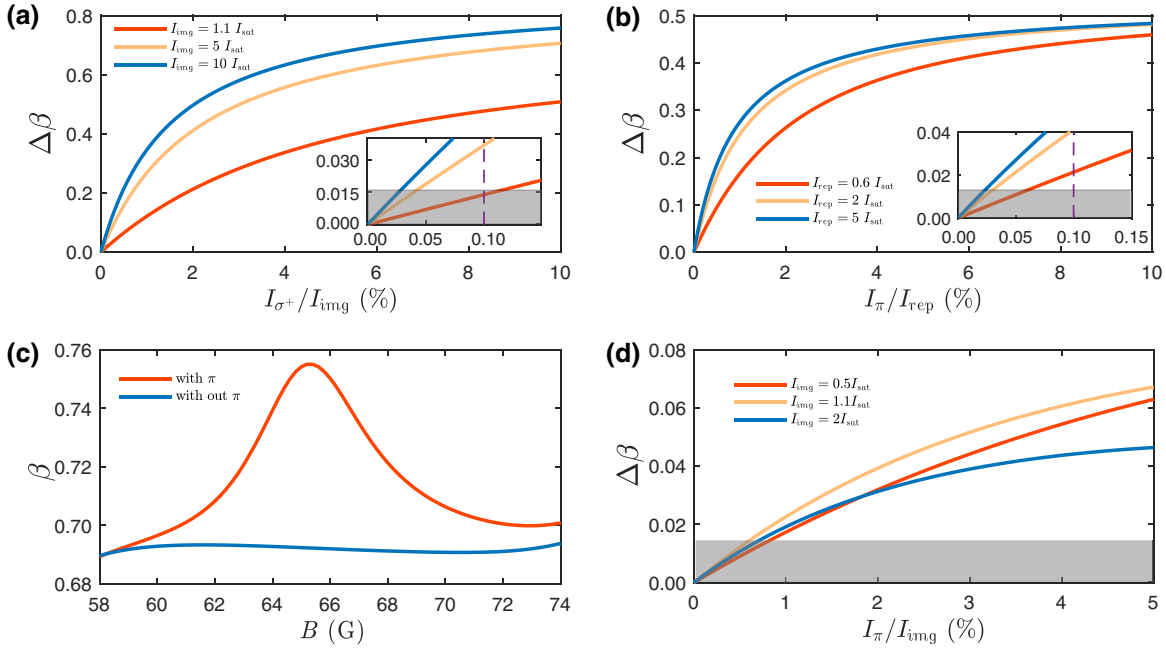

FIG. 5. (a) Variation of β due to different fractions of σ^+ polarization of the imaging light at various intensities of the imaging light under a magnetic field of 51 G. (b) Variation of β due to different fractions of π polarization of the repumping light at various intensities of the repumping light under a magnetic field of 161 G. The shaded region in the inset represents the average error bars of our experimental measurements corresponding to the detection limits of $\Delta\beta$. The dashed purple line in the inset shows that the imperfection of light is at the 0.1% level, which is the performance achieved by commonly used polarizing beam splitters such as Thorlabs PBS102. (c) β versus magnetic field for the imaging light with 4% π polarization (solid red line) or no π polarization (solid blue line). The repumping channel is $5S_{1/2}|\tilde{2}, -\tilde{2}\rangle \rightarrow 5P_{3/2}|\tilde{4}', -\tilde{3}'\rangle$. The π-polarization component increases β because of the energy crossing of the transitions $5S_{1/2}|\tilde{3}, -\tilde{3}\rangle \rightarrow 5P_{3/2}|\tilde{4}', -\tilde{4}'\rangle$ and $5S_{1/2}|\tilde{3}, -\tilde{2}\rangle \rightarrow 5P_{3/2}|\tilde{3}', -\tilde{2}'\rangle$ at a magnetic field of 65 G. (d) At a magnetic field of 65 G, we simulate $\Delta\beta$ versus the π-polarization component of the imaging light. Our resolution limit is at $\Delta\beta \sim 0.015$, and we can resolve the relative intensity at the 1% level.

and is due to the residual π component of the repumping light.

On the basis of these structures, we fit the polarization impurity and find that the π component of repumping light is 0.35%, which is consistent with our other independent polarization measurement at the 0.2% level. The σ^+ component of imaging light is about 3%. These features suggest that we should avoid any Zeeman level crossing during the absorption imaging. Also the imaging transition and the repumping transition should be carefully chosen to get the greatest imaging efficiency.

IV. APPLICATION

In this section, we suggest a practical application of our high-field-imaging model for calibrating the laser-beam polarization by atoms.

As shown in Fig. 4, a slight σ^+ polarization of the imaging light can lead to a significant valley of β at 51 G, while π polarization of the repumping light can result in a peak at 161 G with repumping light at 5 MHz. Therefore, we can use the variation of β to calibrate the polarization quality of both the imaging light and the repumping light.

We define $\Delta\beta$ as the change in β caused by imperfections in the light sources, and we show the corresponding curve in Fig. 5. Within the error bars of our experiment, we can detect imperfections as small as 0.04% for σ^+ polarization of the imaging light with $I_{img} = 5I_{sat}$ and 0.02% for π polarization of the repumping light with $I_{rep} = 5I_{sat}$. To our knowledge, most commercial polarizers, such as Thorlabs PBS102, can provide an extinction ratio of only 1000:1 at the transmission port. Our measurement based on the spectrum can provide higher precision for calibrating the polarization of incident light.

Meanwhile, we also attempt to use this method to calibrate the relative angle θ between the imaging beam and the magnetic field direction. A small relative angle θ causes a fraction $\sin^2\theta/2$ of the π polarization in the total intensity of the imaging beam. As illustrated in Figs. 5(c) and 5(d), the π polarization causes a change of β at a magnetic field of 65 G. As the sensitivity of $\Delta\beta$ is 0.015, we can resolve the smallest relative fraction at 1%, corresponding to an angle sensitivity of 8°. However, it is not an ideal method for fine-tuning the relative angle θ. Our experimental system has a relative angle smaller than 1°, which can be verified by a level meter.

V. CONCLUSIONS

To sum up, we develop a theoretical model that accurately describes the absorption imaging of atoms in the presence of a magnetic field. Our model allows the determination of a correction factor for atom-number measurements and identification of optimal imaging parameters. Our experimental verification of the model shows that absorption spectroscopy provides a sensitive and useful tool for benchmarking laser-beam quality, allowing the detection of features such as polarization imperfections and Zeeman level crossings. This method will be helpful for experimental groups in calibrating absorption imaging and ensuring high-polarization-quality incident light.

ACKNOWLEDGMENTS

This work was financially supported by the National Natural Science Foundation of China (Grants No. 61975092, No. 92165203, and No. 11974202) and the National Key Research and Development Program of China (Grants No. 2021YFA0718303 and No. 2021YFA1400904).

[1] O. Morsch and M. Oberthaler, Dynamics of Bose-Einstein condensates in optical lattices, Rev. Mod. Phys. **78**, 179 (2006).
[2] I. Bloch, J. Dalibard, and W. Zwerger, Many-body physics with ultracold gases, Rev. Mod. Phys. **80**, 885 (2008).
[3] I. Bloch, J. Dalibard, and S. Nascimbène, Quantum simulations with ultracold quantum gases, Nat. Phys. **8**, 267 (2012).
[4] C. Gross and I. Bloch, Quantum simulations with ultracold atoms in optical lattices, Science **357**, 995 (2017).
[5] F. Schäfer, T. Fukuhara, S. Sugawa, Y. Takasu, and Y. Takahashi, Tools for quantum simulation with ultracold atoms in optical lattices, Nat. Rev. Phys. **2**, 411 (2020).
[6] C. Gross and W. S. Bakr, Quantum gas microscopy for single atom and spin detection, Nat. Phys. **17**, 1316 (2021).
[7] M. H. Anderson, J. R. Ensher, M. R. Matthews, C. E. Wieman, and E. A. Cornell, Observation of Bose-Einstein condensation in a dilute atomic vapor, Science **269**, 198 (1995).
[8] K. B. Davis, M. O. Mewes, M. R. Andrews, N. J. van Druten, D. S. Durfee, D. M. Kurn, and W. Ketterle, Bose-Einstein Condensation in a Gas of Sodium Atoms, Phys. Rev. Lett. **75**, 3969 (1995).
[9] S. Stellmer, B. Pasquiou, R. Grimm, and F. Schreck, Laser Cooling to Quantum Degeneracy, Phys. Rev. Lett. **110**, 263003 (2013).
[10] J. Steinhauer, R. Ozeri, N. Katz, and N. Davidson, Excitation Spectrum of a Bose-Einstein Condensate, Phys. Rev. Lett. **88**, 120407 (2002).
[11] P. T. Ernst, S. Götze, J. S. Krauser, K. Pyka, D.-S. Lühmann, D. Pfannkuche, and K. Sengstock, Probing superfluids in optical lattices by momentum-resolved Bragg spectroscopy, Nat. Phys. **6**, 56 (2010).
[12] Y. Guo, R. M. Kroeze, B. P. Marsh, S. Gopalakrishnan, J. Keeling, and B. L. Lev, An optical lattice with sound, Nature **599**, 211 (2021).
[13] M. Greiner, O. Mandel, T. Esslinger, T. W. Hänsch, and I. Bloch, Quantum phase transition from a superfluid to a Mott insulator in a gas of ultracold atoms, Nature **415**, 39 (2002).
[14] N. Gemelke, X. Zhang, C.-L. Hung, and C. Chin, In situ observation of incompressible Mott-insulating domains in ultracold atomic gases, Nature **460**, 995 (2009).
[15] W. S. Bakr, A. Peng, M. E. Tai, R. Ma, J. Simon, J. I. Gillen, S. Fölling, L. Pollet, and M. Greiner, Probing the Superfluid-to-Mott insulator transition at the single-atom level, Science **329**, 547 (2010).
[16] L. Liang, W. Zheng, R. Yao, Q. Zheng, Z. Yao, T.-G. Zhou, Q. Huang, Z. Zhang, J. Ye, X. Zhou, X. Chen, W. Chen, H. Zhai, and J. Hu, Probing quantum many-body correlations by universal ramping dynamics, Sci. Bull. **67**, 2550 (2022).
[17] C. Chin, R. Grimm, P. Julienne, and E. Tiesinga, Feshbach resonances in ultracold gases, Rev. Mod. Phys. **82**, 1225 (2010).
[18] J. Kinast, S. L. Hemmer, M. E. Gehm, A. Turlapov, and J. E. Thomas, Evidence for Superfluidity in a Resonantly Interacting Fermi Gas, Phys. Rev. Lett. **92**, 150402 (2004).
[19] C. Chin, M. Bartenstein, A. Altmeyer, S. Riedl, S. Jochim, J. H. Denschlag, and R. Grimm, Observation of the pairing gap in a strongly interacting Fermi gas, Science **305**, 1128 (2004).
[20] T. Bourdel, L. Khaykovich, J. Cubizolles, J. Zhang, F. Chevy, M. Teichmann, L. Tarruell, S. J. J. M. F. Kokkelmans, and C. Salomon, Experimental Study of the BEC-BCS Crossover Region in Lithium 6, Phys. Rev. Lett. **93**, 050401 (2004).
[21] M. W. Zwierlein, A. Schirotzek, C. H. Schunck, and W. Ketterle, Vortices and superfluidity in a strongly interacting Fermi gas, Nature **435**, 1047 (2005).
[22] T. Kraemer, M. Mark, P. Waldburger, J. G. Danzl, C. Chin, B. Engeser, A. D. Lange, K. Pilch, A. Jaakkola, H.-C. Nägerl, and R. Grimm, Evidence for Efimov quantum states in an ultracold gas of caesium atoms, Nature **440**, 315 (2006).
[23] T. Lompe, T. B. Ottenstein, F. Serwane, A. N. Wenz, G. Zürn, and S. Jochim, Radio-frequency association of Efimov trimers, Science **330**, 940 (2010).
[24] S. E. Pollack, D. Dries, and R. G. Hulet, Universality in three- and four-body bound states of ultracold atoms, Science **326**, 1683 (2009).
[25] M. Zaccanti, B. Deissler, C. D'Errico, M. Fattori, M. Jona-Lasinio, S. Müller, G. Roati, M. Inguscio, and G. Modugno, Observation of an Efimov spectrum in an atomic system, Nat. Phys. **5**, 586 (2009).
[26] M. W. Zwierlein, C. A. Stan, C. H. Schunck, S. M. F. Raupach, A. J. Kerman, and W. Ketterle, Condensation of Pairs of Fermionic Atoms near a Feshbach Resonance, Phys. Rev. Lett. **92**, 120403 (2004).
[27] T. Stöferle, H. Moritz, K. Günter, M. Köhl, and T. Esslinger, Molecules of Fermionic Atoms in an Optical Lattice, Phys. Rev. Lett. **96**, 030401 (2006).
[28] Y. Kiefer, M. Hachmann, and A. Hemmerich, Ultracold Feshbach molecules in an orbital optical lattice, Nat. Phys. **19**, 794 (2023).

[29] M. W. Zwierlein, C. A. Stan, C. H. Schunck, S. M. F. Raupach, S. Gupta, Z. Hadzibabic, and W. Ketterle, Observation of Bose-Einstein Condensation of Molecules, Phys. Rev. Lett. **91**, 250401 (2003).

[30] M. Bartenstein, A. Altmeyer, S. Riedl, S. Jochim, C. Chin, J. H. Denschlag, and R. Grimm, Crossover from a Molecular Bose-Einstein Condensate to a Degenerate Fermi Gas, Phys. Rev. Lett. **92**, 120401 (2004).

[31] A. Schindewolf, R. Bause, X.-Y. Chen, M. Duda, T. Karman, I. Bloch, and X.-Y. Luo, Evaporation of microwave-shielded polar molecules to quantum degeneracy, Nature **607**, 677 (2022).

[32] L. D. Marco, G. Valtolina, K. Matsuda, W. G. Tobias, J. P. Covey, and J. Ye, A degenerate Fermi gas of polar molecules, Science **363**, 853 (2019).

[33] J. Hu, L. Feng, Z. Zhang, and C. Chin, Quantum simulation of Unruh radiation, Nat. Phys. **15**, 785 (2019).

[34] L. Feng, J. Hu, L. W. Clark, and C. Chin, Correlations in high-harmonic generation of matter-wave jets revealed by pattern recognition, Science **363**, 521 (2019).

[35] C. Eigen, J. A. Glidden, R. Lopes, E. A. Cornell, R. P. Smith, and Z. Hadzibabic, Universal prethermal dynamics of Bose gases quenched to unitarity, Nature **563**, 221 (2018).

[36] Z. Zhang, K. X. Yao, L. Feng, J. Hu, and C. Chin, Pattern formation in a driven Bose–Einstein condensate, Nat. Phys. **16**, 652 (2020).

[37] H. Fu, L. Feng, B. M. Anderson, L. W. Clark, J. Hu, J. W. Andrade, C. Chin, and K. Levin, Density Waves and Jet Emission Asymmetry in Bose Fireworks, Phys. Rev. Lett. **121**, 243001 (2018).

[38] Q. Huang, R. Yao, L. Liang, S. Wang, Q. Zheng, D. Li, W. Xiong, X. Zhou, W. Chen, X. Chen, and J. Hu, Observation of Many-Body Quantum Phase Transitions beyond the Kibble-Zurek Mechanism, Phys. Rev. Lett. **127**, 200601 (2021).

[39] Y.-J. Lin, K. Jiménez-García, and I. B. Spielman, Spin–orbit-coupled Bose–Einstein condensates, Nature **471**, 83 (2011).

[40] L. W. Cheuk, A. T. Sommer, Z. Hadzibabic, T. Yefsah, W. S. Bakr, and M. W. Zwierlein, Spin-Injection Spectroscopy of a Spin-Orbit Coupled Fermi Gas, Phys. Rev. Lett. **109**, 095302 (2012).

[41] L. Huang, Z. Meng, P. Wang, P. Peng, S.-L. Zhang, L. Chen, D. Li, Q. Zhou, and J. Zhang, Experimental realization of two-dimensional synthetic spin–orbit coupling in ultracold Fermi gases, Nat. Phys. **12**, 540 (2016).

[42] Z. Wu, L. Zhang, W. Sun, X.-T. Xu, B.-Z. Wang, S.-C. Ji, Y. Deng, S. Chen, X.-J. Liu, and J.-W. Pan, Realization of two-dimensional spin-orbit coupling for Bose-Einstein condensates, Science **354**, 83 (2016).

[43] J. R. Li, J. Lee, W. Huang, S. Burchesky, B. Shteynas, F. Ç. Topi, A. O. Jamison, and W. Ketterle, A stripe phase with supersolid properties in spin-orbit-coupled Bose-Einstein condensates, Nature **543**, 91 (2017).

[44] A. J. Kerman, V. Vuletić, C. Chin, and S. Chu, Beyond Optical Molasses: 3D Raman Sideband Cooling of Atomic Cesium to High Phase-Space Density, Phys. Rev. Lett. **84**, 439 (2000).

[45] J. Hu, A. Urvoy, Z. Vendeiro, V. Crépel, W. Chen, and V. Vuletić, Creation of a Bose-condensed gas of ^{87}Rb by laser cooling, Science **358**, 1078 (2017).

[46] V. Vuletić, C. Chin, A. J. Kerman, and S. Chu, Degenerate Raman Sideband Cooling of Trapped Cesium Atoms at Very High Atomic Densities, Phys. Rev. Lett. **81**, 5768 (1998).

[47] Y. J. Lin, R. L. Compton, K. Jiménez-García, J. V. Porto, and I. B. Spielman, Synthetic magnetic fields for ultracold neutral atoms, Nature **462**, 628 (2009).

[48] H. Miyake, G. A. Siviloglou, C. J. Kennedy, W. C. Burton, and W. Ketterle, Realizing the Harper Hamiltonian with Laser-Assisted Tunneling in Optical Lattices, Phys. Rev. Lett. **111**, 185302 (2013).

[49] M. Aidelsburger, M. Atala, M. Lohse, J. T. Barreiro, B. Paredes, and I. Bloch, Realization of the Hofstadter Hamiltonian with Ultracold Atoms in Optical Lattices, Phys. Rev. Lett. **111**, 185301 (2013).

[50] C. Cohen-Tannoudji and D. Guéry-Odelin, *Advances in Atomic Physics: An Overview* (World Scientific Press, Singapore, 2011).

[51] B. Yang, Y.-Y. Chen, Y.-G. Zheng, H. Sun, H.-N. Dai, X.-W. Guan, Z.-S. Yuan, and J.-W. Pan, Quantum Criticality and the Tomonaga-Luttinger Liquid in One-Dimensional Bose Gases, Phys. Rev. Lett. **119**, 165701 (2017).

[52] T. Yefsah, R. Desbuquois, L. Chomaz, K. J. Günter, and J. Dalibard, Exploring the Thermodynamics of a Two-Dimensional Bose Gas, Phys. Rev. Lett. **107**, 130401 (2011).

[53] P. Christodoulou, M. Gałka, N. Dogra, R. Lopes, J. Schmitt, and Z. Hadzibabic, Observation of First and Second Sound in a BKT Superfluid, Nature **594**, 191 (2021).

[54] L.-C. Ha, C.-L. Hung, X. Zhang, U. Eismann, S.-K. Tung, and C. Chin, Strongly Interacting Two-Dimensional Bose Gases, Phys. Rev. Lett. **110**, 145302 (2013).

[55] C.-L. Hung, X. Zhang, N. Gemelke, and C. Chin, Observation of scale invariance and universality in two-dimensional Bose gases, Nature **470**, 236 (2011).

[56] K. Hueck, N. Luick, L. Sobirey, J. Siegl, T. Lompe, H. Moritz, L. W. Clark, and C. Chin, Calibrating high intensity absorption imaging of ultracold atoms, Opt. Express **25**, 8670 (2017).

[57] G. Reinaudi, T. Lahaye, Z. Wang, and D. Guéry-Odelin, Strong saturation absorption imaging of dense clouds of ultracold atoms, Opt. Lett. **32**, 3143 (2007).

[58] D. A. Steck, Rubidium 85 D line data, available online at: https://steck.us/alkalidata, (reversion 2.2.3, 9 July 2021).

[59] Y. Liu and S. Miao, High-Magnetic-Field-Imaging, code available online at: https://github.com/LiuYuqi19/High-Magnetic-Field-Imaging.git.